

On the effect of Edge vs bulk effects in Graphene Nanoribbons

C. Durkan, X. Liu & E. Saunders

Abstract.

Recent works have shown how the electrical properties of graphene nanoribbons (GNRs) show a size-dependence in terms of resistivity, charge neutrality point (CNP) and band structure once their widths drop below approximately 50 nm. It has been observed that the CNP switches sign below a certain GNR width, and in this article, we explore this via computational modelling of the electric field and the conductance of GNRs in the presence of an AFM tip. We show that CNP is expected to shift towards lower values as GNR width reduces as a result of the significantly enhanced electric field around edges, but that a change in sign is not expected. We also show experimentally via high-resolution Scanning Gate Microscopy (SGM) that there does not appear to be any significant difference between the edges and the bulk of a GNR, indicating that the switch in CNP is not due to differential doping, and may instead be due to variations in the band structure as a function of size.

1 Introduction

There have been significant efforts over the past 2 decades in developing novel electronic and optical devices using graphene. However, there are a number of well-known limitations which need to be overcome with intrinsic graphene including (i) the absence of a bandgap, resulting in low on/off current ratios, rendering it impractical as a candidate material for transistors and (ii) its low conductivity and carrier density. However, the first of these issues can be addressed as a bandgap can be artificially induced via quantum confinement by constricting graphene laterally, i.e. by forming graphene Nanoribbons (GNRs) [1-3], by imposing a periodic potential [4-6], or by using twisted bilayers [7].

A previous experimental study [3] on GNRs demonstrated a width-dependent shift of the charge neutrality point (CNP) from positive to negative as the width reduced below a certain value dependent on the geometry of the device, but typically in the range of a few 10s of nm. This led to the hypothesis that graphene nanoribbons fabricated using oxygen plasma treatment have n-type edges and a p-type bulk. In this article, we directly investigate this via a combination of Scanning Gate Microscopy and modelling.

The width, edge structure and doping of a graphene nanoribbon affect the bandgap and the overall electrical properties and this can be exploited in the fabrication of devices in order to tailor device characteristics and performance. However, in order to achieve a bandgap

comparable to that of Silicon, widths somewhat below 10 nm are required, mostly necessitating the use of resist-based patterning techniques. It was shown [1] that even 10-nm wide GNRs have a relatively small bandgap in the range 100-200 meV, as compared to Silicon's value of 1.12 eV. Another issue is that the fabrication methods used to create nanoribbons can introduce significant edge defects which affect the transport properties and reduce the high charge carrier mobility that is possible in graphene. It is therefore highly unlikely that any such device architectures will be practical to implement at scale unless the edge structure can be characterised and controlled. Nonetheless, there is much that can be learned about electronic systems at reduced lengthscales by exploring such devices, which may be applicable more broadly.

In practice, graphene's sensitivity to defects – even including the presence of an underlying substrate – prevents it from achieving its theoretical potential. Nonetheless, carrier mobilities of up to $180000 \text{ cm}^2\text{V}^{-1}\text{s}^{-1}$ have been demonstrated for graphene at room temperature on a hBN substrate [8]. This is still significantly higher than the values of $1500 \text{ cm}^2\text{V}^{-1}\text{s}^{-1}$ and $450 \text{ cm}^2\text{V}^{-1}\text{s}^{-1}$ for electrons and holes respectively in intrinsic Si [9]. Other exceptional electronic properties thus far observed in graphene are carrier mean free paths in excess of $1 \mu\text{m}$ [10], drift velocities of the order of 10^7 cm/s [11], and breakdown current densities in the order of 10^8 A/cm^2 [12] in GNRs, the latter of which is comparable to high-quality metallic nanowires [13].

Defects play a significant role in determining the overall electrical properties of graphene, beyond GNRs, as can be seen by the fact that the conductivity at the Dirac point in real devices has been measured as being approximately $\frac{4e^2}{h}$ as opposed to zero as would be expected from the band structure of pristine graphene. It has been proposed that this is due to the rippling of the graphene sheet and impurities from underlying substrates that create puddles of carriers for conduction [14].

The surface of graphene is typically covered with adsorbates comprising contaminants from the atmosphere and chemical residues from device fabrication. These defects have the effect that graphene is often unintentionally doped (mostly p-type), with typical measured carrier densities in the range $10^{11} - 10^{12} \text{ cm}^{-2}$ [10, 15]. The consequence of this is not only a higher conductance: careful choice of metal electrode material is required to avoid a Schottky-type contact and significant band bending. Even in the absence of any ambient contaminants, the underlying substrate can influence the doping of graphene – for instance graphene on pristine SiO_2 has been shown to be n-type [16].

In terms of previous work on GNRs, it has been demonstrated that the bandgap, ΔE , scales with the width, w , of a nanoribbon as $\Delta E \propto 1/w$. This dependence further illustrates the expected Dirac-like Fermion nature of the charge carriers as opposed to Schrödinger particle-in-a-box behaviour which would lead to $\Delta E \propto 1/w^2$. The edge structure, i.e. armchair or zigzag is critical in determining the GNR's properties. Numerical simulations show [17] that zigzag ribbons are expected to have no bandgap whereas armchair ones do (with the above width-dependent bandgap), but due to the computational cost of such calculations, the widest GNRs that have been simulated atomistically thus far are typically just a few nm wide, which is smaller than can be reliably fabricated. For this reason, we present a mesoscopic continuum model which is able to reproduce many of the key experimental features and which is useful for interpreting our results. This model is implemented in COMSOL Multiphysics [18], where drift-diffusion equations can be used to model the transport in graphene devices as long as the channel length is longer than the mean free path [19], i.e. where the transport is not ballistic.

Previous experimental work [3] investigated the effect of the width of GNRs on their resistivity. The results showed the trend of the resistivity increasing as the width decreases, particularly below widths of around 50 nm. The rate at which resistivity increases with decreasing width was shown to be much faster than for the case of metallic nanowires where resistivity scales as $1/w$ once the width decreases below the bulk mean free path [13]. It was shown that this difference in behaviour is due to a combination of (i) fabrication methods causing a high degree of edge disorder and therefore primarily diffuse scattering at the edges and (ii) deviations in the bulk band structure starting to become noticeable, with the emergence of a bandgap and subsequent suppression of carrier density. As width reduces, edge scattering effects become more prominent and so the mean free path reduces and the resistivity increases. It was also observed that the CNP switched polarity at a width of around 50 nm where the ribbons are predominantly p-type above 50 nm and n-type below 50 nm. The precise value of the width (which we will call the crossover width) at which this switch occurs varies as the underlying oxide thickness varies (thinner oxide layers lead to narrower crossover widths) and with the process conditions used to fabricate the GNRs. One would expect that this crossover is associated with changes in charge carrier distribution, which is something that can be visualised by using Scanning Gate Microscopy (SGM) measurements using an Atomic Force Microscope (AFM). Jalilan *et al* used SGM to spatially map puddles of electron and hole concentrations in a Graphene field effect transistor sample, with a spatial resolution of order $1 \mu\text{m}$ [20]. These charge puddles were likely from dopant sources such as metal contacts, surface contaminants and edge effects.

In this article, we report on the use of much higher resolution SGM measurements to map variations in the charge carrier density in graphene nanoribbons with the aim of visualising whether there is a p-type bulk and n-type edges that would explain the observed CNP characteristics.

2 Apparatus and Experimental Techniques

In scanning gate microscopy, an electrically conductive AFM tip is used as a local top gate to map the conductance characteristics of an underlying sample. A voltage bias is applied to the tip which leads to a modification of the local carrier density in the sample immediately below it via the field effect. It is important to note that the tip and sample are not in Ohmic contact (either by operating in non-contact mode or by having a thin insulating layer on the surface), so there is no direct transfer of charge from one to the other. The resultant changes in local carrier concentration alter the conductance of the sample, which can be measured as a change in current in a Field-effect Transistor (FET) configuration, i.e. where Source and Drain metal contacts are added across the sample. Whether the current increases or decreases is determined by whether the tip enhances or depletes the hole or electron carrier density, allowing the local carrier type to be determined. A back gate is used to bias the sample to near the CNP in order to optimise the signal to noise ratio of the change in current induced by the scanning top gate (the AFM tip). There are two modes in which SGM can be used – (i) fixed bias and (ii) fixed-tip, both of which were employed in this work. In these modes, changes in the current passing through the sample are measured as a function of the tip bias or position. The spatial resolution of SGM will depend on the tip size and shape, the tip voltage and the tip-sample distance, as well as on the diffusion length of the charge carries in the sample, similar to what is seen with scanning spreading resistance microscopy [21].

In fixed bias mode, the AFM operates in tapping mode, and the tip is held at a fixed DC voltage bias. For each tip location, the current flowing through the sample is measured and logged. A current map is therefore collected at the same time as the topography and the two can be correlated. This is generally repeated for a number of different tip voltages and average tip-sample distances.

In fixed-tip mode, the AFM tip is held (usually a few 10s of nm) above the sample at a specific location and the current through the sample is measured as a function of the tip voltage. As in fixed-bias mode, the tip voltage leads to an enhancement or depletion of

the charge density in the sample. The difference between the tip voltage and the back-gate voltage at which the current through the sample (from Source to Drain) reaches its minimum value is the local CNP. The polarity of this local CNP tells us whether the area directly under the tip is p-type or n-type so by performing this SGM measurement at different points in the sample, information about the spatial variations in the majority carrier types can be gained.

The setup that was used, as well as the device architecture are shown in Figure 1(a). The samples were mounted in a miniature probe station that was built on the AFM sample scanning stage. The AFM tip (top gate) voltage, V_{tg} , and the back gate voltage, V_{bg} , were independently set. Using conductive BeCu probes with a nominal radius of 5 μm , the GNR was grounded at one end and a small voltage, V_s was applied to the other end. The resulting current flowing through the sample, I_s , was collected using a Femto DLPCA-200 variable gain, low noise current-voltage convertor, the output of which was fed to the input of an analog to digital convertor (ADC) in the AFM controller. This was used with a transconductance of 10^7 V/A and a 50 kHz bandwidth.

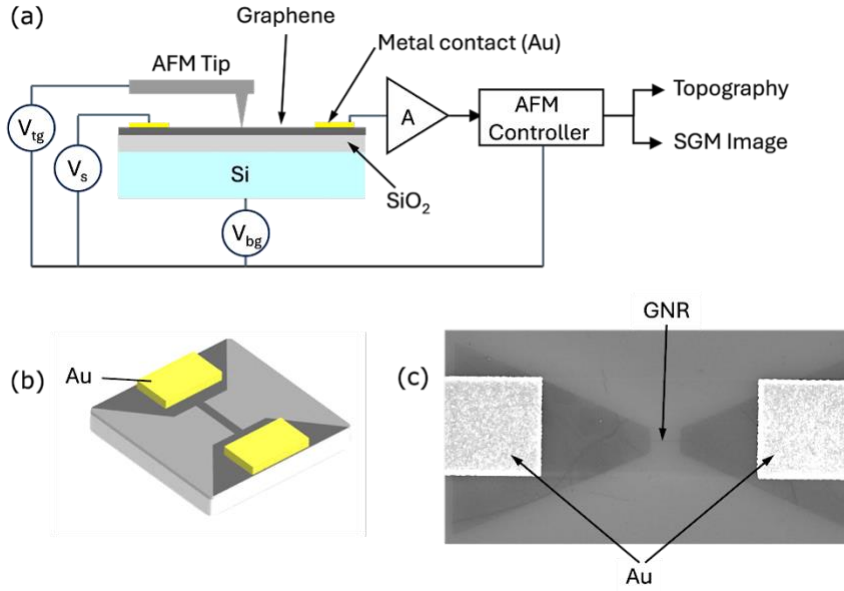


Figure 1: (a) Experimental set-up for Scanning Gate Microscopy (SGM) where V_{tg} , V_s , and V_{bg} are the top gate voltage (applied to the tip), source voltage and back gate voltage and “A” is a transimpedance amplifier; (b) device layout – the Au is deposited directly on graphene with a Cr adhesion layer, and creates the source and drain contacts; (c) example device with a 15 nm wide GNR. The devices are symmetric, and the source and drain contacts are on the left and right, respectively.

A Park Systems XE-100 AFM was used for these experiments. This is a sample-scanning system where the sample stage has sufficient access to allow for a miniature probe station to be mounted on it. The optical Microscope of the AFM was used with a $5 \times$ objective lens which combined with the other optical components gives a magnification of $500 \times$. This was used to locate the AFM cantilever and position it above the relevant GNR as well as to position the probes on the source and drain contacts. The AFM tips used were model Multi75E-G with a nominal stiffness of 2.8 N/m , resonance frequency of 75 kHz and with an electrically conductive coating of 5 nm chromium and 25 nm platinum to give a radius of curvature at the tip apex of approx. 25 nm .

The GNRs were fabricated using the multistep process outlined in reference [3], and all samples were prepared with an alumina passivation layer approximately 7.5 nm thick. This prevents deterioration over time and ensures there are no accidental short-circuits between the tip and sample. The fabrication involves the use of an O_2 plasma to remove any unwanted graphene, and it is known that this will lead to a variety of C-O species at the edge, and typically leads to edges being doped p-type [22]. After fabrication and before being placed in the AFM, the transconductance of the GNRs was measured using a Keithley 4200 Source measure unit with a vacuum probe station (Lakeshore) operating at room temperature and a modest vacuum of $3 \times 10^{-4} \text{ mbar}$. It is worth noting that for the work presented in [3], the underlying oxide had a thickness of 300 nm , whereas for the devices presented here, the oxide was 90 nm thick. This has the effect of reducing the crossover width at which the CNP appears to switch sign. An illustration of the device layout is shown in Figure 1(b) indicating the Source and Drain contacts, and an SEM image of a device is shown in Figure 1(c) where the $5 \text{ nm Cr}/25 \text{ nm Au}$ Source (left) and Drain (right) contacts can be clearly seen.

3 COMSOL Model

In order to be able to model the coarse electrical behaviour of the GNR devices, the semiconductor module of COMSOL was used. Given that COMSOL does not have a built-in model for graphene and an atomistic simulation would be too computationally costly, it was modelled as a thin 3D semiconductor with a near zero bandgap. We solved the Poisson equation and concentrated on the overall trends of the mesoscopic behaviour without explicitly including any quantum components. We would expect the model to be reasonably accurate down to widths in the range $10\text{-}20 \text{ nm}$ below which quantum effects and bandgap

variations are known to become significant. We have also not taken account of the atomic nature of the edges, nor whether they are armchair or zig-zag.

The transport physics is based on the drift-diffusion (DD) model, the validity of which will start to break down for GNR lengths shorter than the mean free path due to the appearance of nonstationary and/or quasi-ballistic transport effects. However, some models suggest that by assuming a modified gate-length-dependent saturation velocity, DD provides reasonable results for smaller lengths [23]. Even without this modification, the DD approach is considered a reasonable guide even in the presence of nonstationary and quasi-ballistic transport in short-channel MOSFETs since it correctly accounts for both device geometry and electrostatics. Nonetheless, the devices we reported on in reference [3] are sufficiently large that this modelling approach should be appropriate.

A summary of the material properties used for modelling the graphene is given in Table 1. The dielectric constant of 8 was assumed based on reported experimental measurements on Graphene [24]. Similarly, the mobilities were determined experimentally from conductance measurements on the GNRs [3]. The bandgap was set to a constant value less than $k_B T$. This approach was necessary as if the value 0 is used, COMSOL was unable to converge on a solution. The acceptor doping level, N_A was chosen to give good agreement with measured current-voltage characteristics for bulk graphene devices (we tested graphene with lateral size 5 $\mu\text{m} \times 25 \mu\text{m}$).

Property	Value
Relative Permittivity	8
Bandgap	5 meV
Electron Mobility	3000 cm^2/Vs
Hole Mobility	3000 cm^2/Vs
Acceptor dopant concentration, N_A	$1 \times 10^{12}/\text{cm}^{-2}$

Table 1 - Graphene Material Properties used in COMSOL simulations

The DoS was simply copied from the built-in Si material, but with 1/10th of the N_V and N_c used. To avoid voltage offsets from work function differences, the contacts were set to have an equal nominal work function to graphene. The justification for this comes from the fact that

experimentally, the contacts are clearly Ohmic with no evidence of any Schottky-like behaviour.

The geometry of the modelled system can be seen in Figure 2. The graphene layer is 1nm thick which was chosen as a suitable minimum value due to the constraint it puts on the size and therefore number of elements needed in the mesh. The AFM tip was modelled as a sphere with a diameter of 35 nm. It was treated as an internal boundary with an applied electric potential rather than as a metal or semiconductor domain in order to reduce the model complexity.

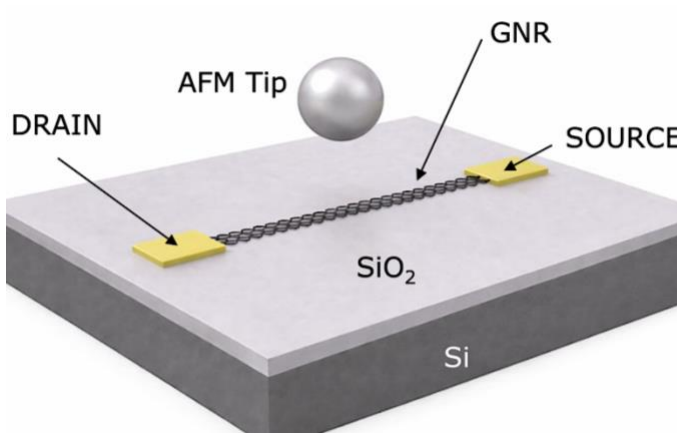


Figure 1: Schematic of the system modelled in COMSOL, where the AFM tip is approximated by a sphere for simplicity.

An infinite-element domain was used at the majority of the boundaries to minimise the variation in results with modelled domain size. Instead of modelling doped Si, the substrate/back-gate was modelled as a boundary at constant electric potential. This approach was taken as the semiconductor regions are the most computationally intensive part of the model for achieving solution convergence.

The drain and source terminals to the GNR were modelled as metal contacts to reduce the physical size of the model, instead of the graphene wedge structure present in the real devices (see Figure 1(b)). Despite the fact that the nominal work functions are equal, this still leads to carrier injection and some band-bending in the GNR within the vicinity of the contacts which then imposes a minimum length limit on the GNRs to be simulated to avoid behaviour being significantly impacted by this region. The region with band-bending was seen to extend out to around 10 nm from the contact, so the minimum length GNR which was simulated was

chosen to be 100 nm. Increasing the length of the GNR increases the number of elements required to produce a suitable mesh. Given that the computational cost of the simulations scales with the number of degrees of freedom in the problem, which is proportional to the number of elements used, the maximum length (or width) of ribbons we investigated was 400 nm.

It is also worth noting that the element size in the graphene should be smaller than the Debye (Thomas-Fermi) screening length as the graphene is being modelled as a semiconductor. This is automatically managed within COMSOL and is of order 5 nm for the chosen parameters in Table 1.

4 Results and discussion

COMSOL Simulations

The first step was to simulate the field-effect conductance of a device in the absence of an AFM tip, as shown in Figure 3. The back-gate voltage was swept for a number of GNR widths from 10-400 nm. The oxide thickness used was 90 nm and the same doping concentration of 10^{12} cm^{-2} was used for each device, as per the figures in Table 1. Similar results are seen with a reversed back-gate voltage polarity if n-type doping of the same concentration is modelled. For computational efficiency, this set of simulations used different lengths for different widths, so to facilitate comparison, conductivity has been plotted instead of current.

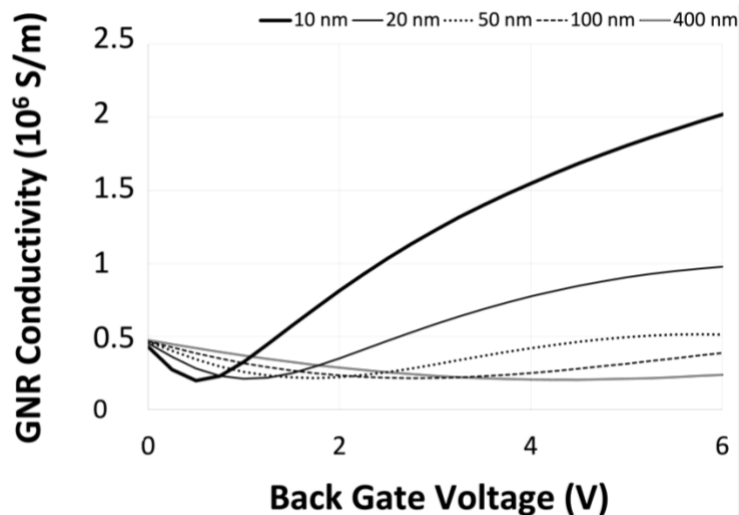


Figure 3: Simulated global gate effect with varying GNR width, showing that the Charge Neutrality Point (CNP) shifts towards zero as GNR width is reduced.

As is clear from this, the CNP shifts towards lower voltages as the width is reduced. In broad terms, this is similar to what was experimentally observed [3], although in the simulations, there is no evidence of a crossover, i.e. the sign of the CNP does not change. Given that the edges are modelled as having the same doping density as the bulk of the GNR, the observed shift of the CNP in Figure 3 is therefore not consistent with the hypothesis from reference 3 that the GNR edges are n-type. Instead, what we are observing is the effect of fringing of the electric field. These results can be explained by thinking of the GNR and back gate as the plates of a parallel plate capacitor, where fringing becomes significant when the lateral size of one or both of the plates becomes comparable to the distance between them. For electrodes which both have a large lateral extent compared to the separation, the electric field between them is essentially uniform. However, when the separation becomes significant compared to the lateral size of the electrodes, the fringing of the electric field at the edges of the plates can dominate the behaviour.

For the GNR-FETs, this has the consequence that the CNP of wider ribbons such as the 400 nm wide GNR in Figure 3 converges to that seen for bulk devices.

In any FET, it is the gate electric field rather than the gate bias that determines the device behaviour. As a result of fringing, the field distribution is significantly altered in small GNRs relative to larger ones, leading to a different distribution of charge and ultimately, a different conductivity.

The simulations (and experiments) show that the field-enhancement around the edges is high enough that the CNP ends up reducing as width is reduced, i.e. the maximum depletion of the charge carriers can be achieved for a lower voltage for narrower GNRs. The field resulting from two different GNR widths can be seen in Figure 4 where we show a cross-section taken through the GNRs halfway along their length. In this figure, we show a zoom-in of the GNRs with widths of (a) 25 nm and (b) 400 nm.

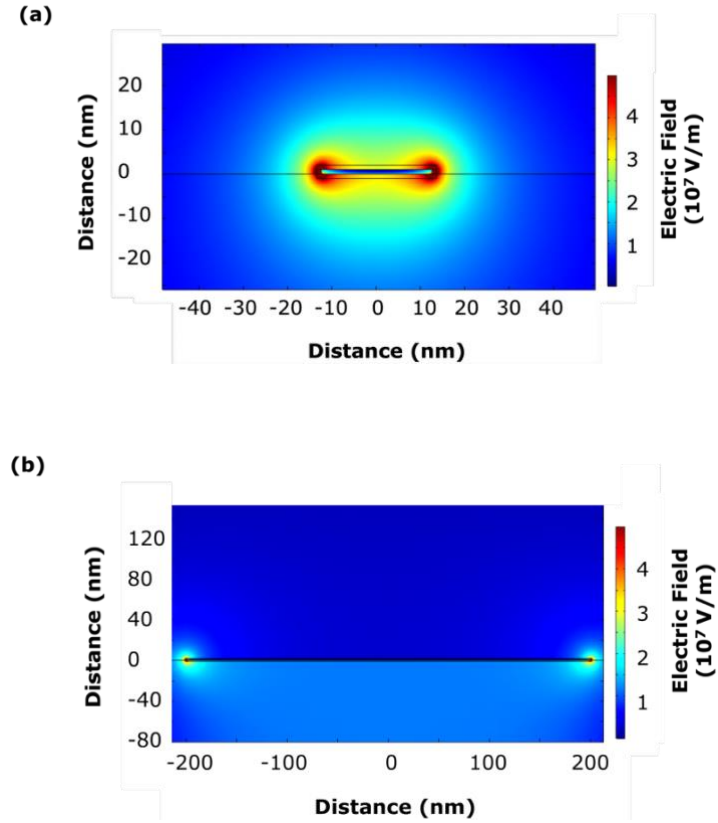


Figure 4: Electric field strength in cross-sections of GNRs (looking along the length axis) of width (a) 25 nm and (b) 400 nm for a back-gate bias of 1 V and an underlying SiO_2 layer of thickness 90 nm.

The differing degree to which fringing occurs in the 2 GNRs is immediately apparent., with strong field enhancement evident in the narrower one. It can also be seen that the field enhancement originates at the edges, where there are high spatial variations in potential by virtue of the geometry. The narrower GNR can be seen to have a greater average field than the wider GNR due to the more prominent fringing, therefore modulating the carrier density more strongly for the same bias, especially at the edges due to the high spatial curvature there. As can be seen in Figure 5, the effect of this field enhancement is that the edges have a higher concentration of electrons than the bulk and effectively behave as n-type. However, this fringing effect does not cause the CNP to switch sign, so it cannot fully account for the observations in ref [3]. The inversion of the charge carriers at the edges is therefore entirely a field effect and is dependent on the applied bias, so cannot be considered to be equivalent to doping.

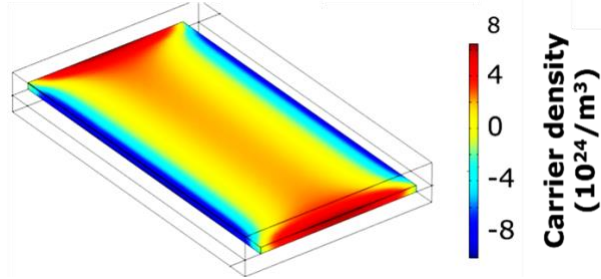


Figure 5: Signed carrier distribution for GNR of width 25 nm at back-gate bias of 1 V. The red areas indicate majority p-type carriers and the blue areas indicate majority n-type carriers.

We then investigated the expected result of the two SGM modes discussed above, for the case of a 50 nm wide GNR with an AFM tip present, which can act as a scanning top gate. A back-gate bias of either +1 V or -1 V was used. For the fixed tip position simulation, the tip was positioned in the centre of the GNR with a 10 nm gap between the bottom of the AFM tip and the top of the oxide surface. For the fixed bias simulation, the tip was kept at the same height but with a bias of either +1 V (the local CNP voltage when positioned over the centre of the GNR), +2 V or +4 V, and the centre of the tip was then moved laterally across the GNR starting from 130 nm from the centre (105 nm from the edge) to the opposite side, passing above the centre of the device, while calculating the drain current at each position. The predicted variation in current for the fixed tip position and fixed tip bias SGM modes are shown in Figure 6 (a) and (b), respectively.

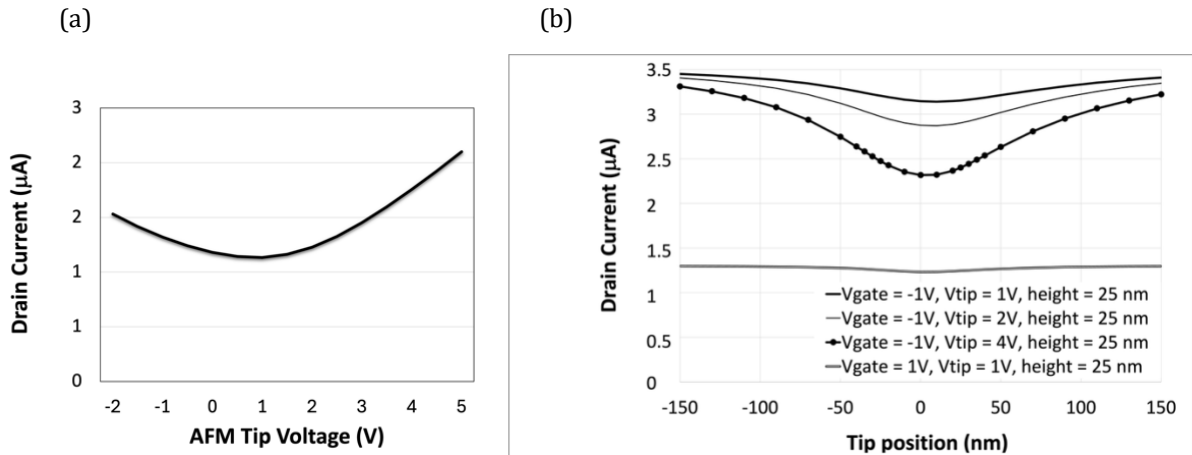


Figure 6(a): SGM simulation of fixed tip mode for the tip above the GNR centre showing the effect of sweeping the tip bias on the GNR current, (b) SGM simulation of fixed bias mode for both fixed tip and sample biases where x = 0 nm is the centre of the GNR (width 50 nm)

These plots show that the order of magnitude maximum variation in current to be expected using the SGM technique is in the range of 10-20%. However, the simulated nanoribbon here

is 100 nm long due to computational constraints whereas the actual GNRs that we fabricated are around 600 nm long. Therefore, the simulations would be expected to overestimate the gate effect from the tip by a factor of around 6.

The average height of the tip above the surface and the tip radius both influence the magnitude of the corresponding electric field in the GNR, and therefore have a significant effect on the current, as shown in Figure 7. The simulation shows the expected variation in current for a 15nm radius tip with a 10nm gap and then a 25nm radius tip with 10nm and 20 nm gaps. A larger tip gives rise to a larger change in current, but the spatial resolution is clearly lower, as the edge sharpness is reduced when compared against the smaller tip. Increasing the gap between the tip and sample also has the effect of reducing the overall change in current and smears out the edge even further. In other words, to be able to observe the fringing-induced carrier distribution at the edge, the AFM tip will need to be as small as possible and as close as possible to the surface of the GNR to create a highly-localised field, entirely in line with what one would expect. The value of the simulations is that it allows us to design the experiment accordingly, which we will now consider.

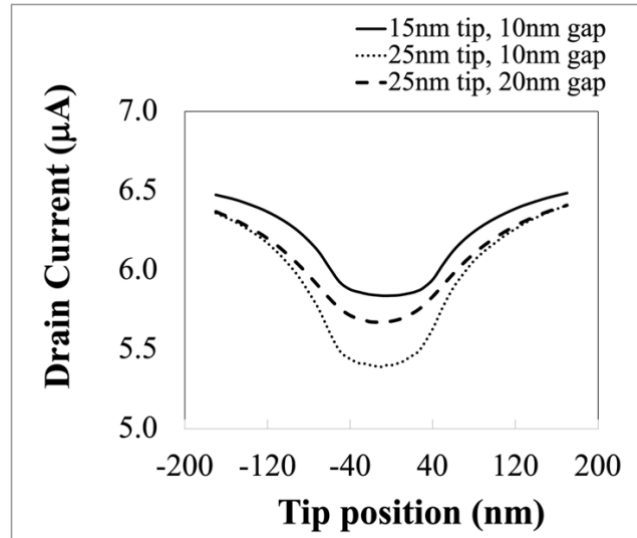


Figure 7: COMSOL simulation of drain source current results with varying AFM tip radius and two different tip heights where $x = 0$ nm is the centre of the GNR.

In the next section, the correlation between experimental results and the above simulations will be examined.

Experimental results

It has been seen previously that GNRs made using the process employed in this work typically appear to switch their majority dopant type at a width of around 50 nm, with GNRs seemingly being n-type below 50 nm and p-type above it. The GNRs used here were deposited on a 90 nm oxide layer as opposed to the 300 nm one used in [3] so we would expect to see the corresponding shift in CNP to only become apparent for smaller widths. As a rough estimate, based on geometric scaling, the crossover point should be of order $50 \times \frac{90}{300} = 15$ nm.

The expected trend of reducing CNP with reduced GNR width is indeed apparent from Figure 8 where we show the results of a back gate voltage sweep for GNR FETs with widths ranging from 27nm to 320nm. However, no switch in polarity is observed for the narrower GNRs, as they are not narrow enough, consistent with the hypothesis that the switch is related to the effect of fringing fields rather than being due to there being a dramatically different structure at the edges. For comparison, the simulated values of CNP, as extracted from figure 3 are shown in Figure 9. It is clear that the overall trends of both theory and experiment are roughly the same and that agreement is reasonable for mid-range widths, but they start to deviate noticeably for widths below around 50 nm. The simulation predicts a stronger dependence on width than is observed experimentally.

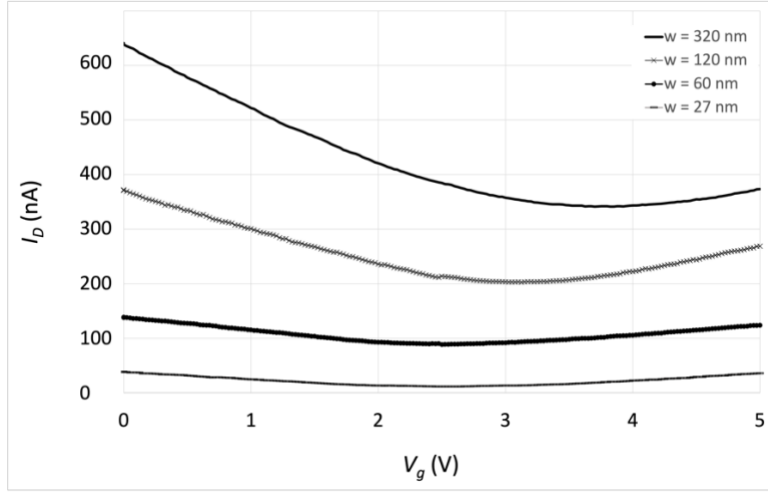


Figure 8: Experimental Measurement of Drain Current Vs back gate voltage for different GNR widths, showing the shift of CNP towards lower values as width decreases.

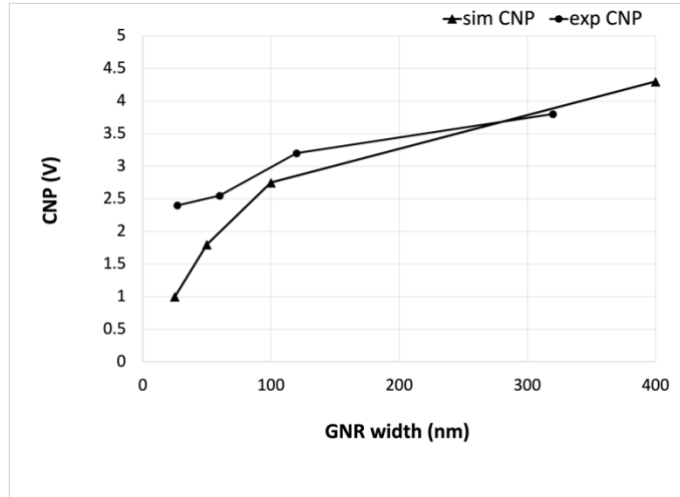


Figure 9: Comparison of simulated (sim) and Experimental (exp) values of CNP for different GNR widths, in the absence of the AFM tip top-gate.

In order to explore the nature of the edges in more detail, we then carried out Scanning Gate Microscopy.

AFM – SGM measurements

SGM was carried out with -1V applied to the back gate. The experiments presented here were carried out on two GNRs which were nominally 120 nm wide and 600 nm long. In Figure 10, we show a map of the change in current overlaid on the topography image, clearly demonstrating that there is a gate effect which is localised to the GNR.

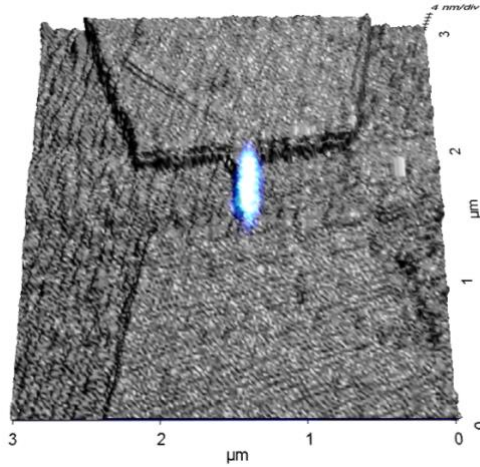


Figure 10: 3D render of change in current on the AFM topography illustrating the spatially-localised gate effect of the tip

In Figure 11, we plot the change in current for both GNRs, where each was measured using a different AFM tip with different apparent radius. In both figures, the baseline Drain-Source current is 600 nA. The free oscillation amplitude of the AFM tip is 33 nm and the oscillation setpoint is set at 16 nm. The average distance between the tip apex and the sample is of order 15-16 nm. In Figure 11(a), we show results from an experiment where the tip voltage was held at +2 V. There is some contamination on the GNR which is a residue from the various lithography processes used to fabricate it, hence the measured height of approximately 15 nm as opposed to the expected value of order 7.5 nm. This, combined with the average tip-sample separation means we would expect the simulations for tip-sample distances in the range 15-30 nm to be appropriate. It is worth pointing out that contact-mode AFM is often employed to mechanically clean graphene surfaces and devices, but for the devices reported here this was not possible without causing irreversible damage to the GNRs given their small size.

There is no reversal of the change in current in the vicinity of the edge and therefore no evidence of a transition from *p* to *n* type. However, there is a clear step in the current change when the edge of the tip passes over the edge of the GNR in Figure 11(a), as indicated by the arrows. The overall change in current measured when the tip passes from the centre of the GNR to 100 nm from the edge is of order 12 nA, which corresponds to a change of around 2%. The edge sharpness of the topography image is approximately 25 nm, indicating a tip radius of the order 25 nm. Then in Figure 11(b), we show data for a larger tip and for two different tip voltages of 1 and 3 V. For the case of 1 V on the tip,

the signal to noise ratio of the change in current is such that only a small difference can be seen as the tip passes over the centre of the GNR. In contrast, the change for a tip voltage of 3 V is significantly larger, and the total change is approximately 40 nA, or 6.7% of the baseline current. The edge sharpness of the topography image in this case is larger at approximately 40 nm, indicating a blunter tip with radius of the order 40 nm. In line with the simulation, this leads to a more noticeable but more smeared out gate effect from this tip.

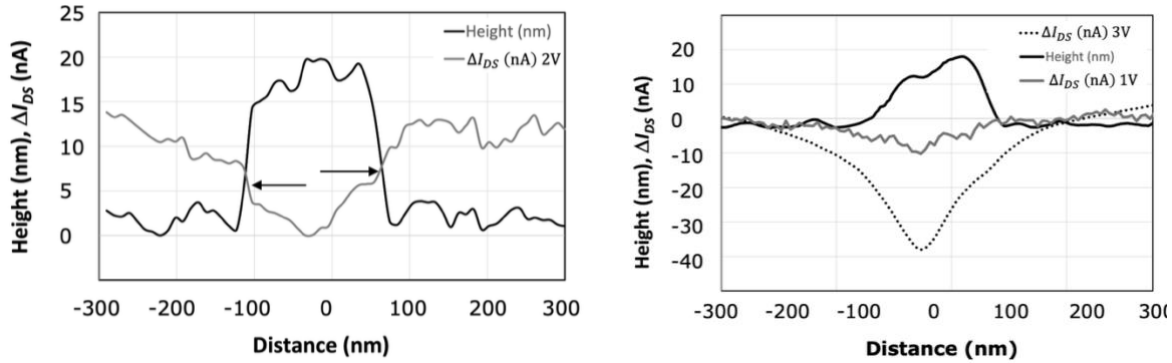


Figure 11: Measured change in current as a function of tip position as it scans across a GNR, with topography cross-section. Both images are for different GNRs of nominal dimensions 120 nm wide and 600 nm long. (a) and (b) were taken with a tip with apparent radius of order 25 nm and 40 nm, respectively. The arrows in Fig. 11(a) indicate where there is a large change in current at the edge of the GNR

An objective of this study was to use SGM to probe the p-type bulk and n-type edges that were hypothesised by Xiao et al [3] as an explanation for the crossover at a width of around 50 nm. We would therefore expect to see a difference in gate effect at the edges of a GNR. This would appear as an increase in current when the tip is at the edge of the GNR where the tip bias was above -1 V (i.e. moving towards 0 V) or a decrease where the tip bias was below -1 V (i.e. more negative than -1 V). It is clear that this is not visible in any of the measurements, although there is a clear kink downwards in the current experienced for the smaller tip as it passes over the edge, starting from the oxide, as shown in Figure 13(a). Given that this is spatially localised to a region approximately 10nm wide centred at the edge, it is most likely a result of a local enhancement of the Electric field when the tip is in close proximity to the edge. We would also expect an upwards rather than downwards kink at this point, which is a strong indicator that the edges truly are not n-type. Given also that (1) there is good agreement between the

simulated and experimental line profiles for current as a function of tip position without including any difference in edge doping and (2) the overall trends of CNP vs width (apart from cross-over) are in good agreement until the GNR width drops below around 50nm at which point the band structure is known to start to deviate from bulk graphene, we must therefore conclude that the shift in CNP polarity for reduced GNR widths is not a result of the doping switching sign from p-type to n-type at the edges, and it must instead be a result of size-induced modifications to the band structure. This would also explain why other electrical measurements that we have performed including Kelvin-Probe Force Microscopy and Electrostatic Force microscopy never reveal any difference in potential or charge density at the edge of graphene as prepared using Oxygen plasma.

Conclusion

We have carried out an experimental and computational study of the effect of GNR width on the spatial distribution of charge density. We show that as a result of geometrically-induced electric field enhancement around the edges of GNRs, there is an inversion of charge located near the edge, which leads to the CNP shifting to lower values. Scanning gate microscopy experiments also indicate that this inversion is a field-effect and is not due to any significant edge doping. We conclude that although the trends we predict are broadly in line with experimental observations, the inversion of the CNP cannot be explained by fringing, and there is no evidence for edge doping, which means that it must instead arise due to some other effect, which is likely to be shifts in the graphene band structure at reduced lengthscales, which is known to be associated with the emergence of a band gap.

Acknowledgement

The authors would like to acknowledge that some developmental work on the COMSOL code was carried out by Anna Mills.

References

- [1] M. Y. Han, B. Ozyilmaz, Y. Zhang, and P. Kim, "Energy band-gap engineering of graphene" nanoribbons," *Phys. Rev. Lett.*, **98**, 206805, (2007).

- [2] P. Jacobse, A. Kimouche, T. Gebraad, M. Ervasti, J. Thijssen, P. Liljeroth, and I. Swart, "Electronic components embedded in a single graphene nanoribbon," *Nature Communications*, **8**, 119 (2017).
- [3] Z. Xiao and C. Durkan, "Size effects in the resistivity of graphene nanoribbons," *Nanotechnology*, **30**, 445203 (2019).
- [4] C. H. Park, L. Yang, Y. W. Son, M. L. Cohen & S. G. Louie, Anisotropic behaviours of massless Dirac fermions in graphene under periodic potentials. *Nat. Phys.* **4**, 213–217 (2008).
- [5] Q. Wan, Z. Xizo, Z. Kursumovic, J. L. MacManus-Driscoll & C. Durkan, "Ferrotronics for the creation of bandgaps in graphene". *Phys. Rev. B*, **107**, 045428 (2023).
- [6] J. A. Briones-Torres, J. Madrigal-Melchor, J. C. Martínez-Orozco & I. Rodríguez-Vargas, Electrostatic and substrate-based monolayer graphene superlattices: Energy minibands and its relation with the characteristics of the conductance curves. *Superlattices Microstruct.* **73**, 98 (2014).
- [7] K. F. Mak, C. H. Lui, J. Shan, and T. F. Heinz, "Observation of an electric-field-induced band gap in bilayer graphene by infrared spectroscopy," *Phys. Rev. Lett.*, **102**, 256405, (2009).
- [8] D. G. Purdie, N. M. Pugno, T. Taniguchi, K. Watanabe, A. C. Ferrari, and A. Lombardo, "Cleaning interfaces in layered materials heterostructures," *Nat. Commun.*, **9**, no.1, 1–12, (2018).
- [9] K. K. Ng & S. M. Sze, *Physics of Semiconductor Devices* - 3rd Edition, New York Wiley, 2006.
- [10] A. S. Mayorov et al., "Micrometer-scale ballistic transport in encapsulated graphene at room temperature," *Nano Lett.* **11**, no. 6, 2396, (2011).
- [11] I. Meric, M. Y. Han, A. F. Young, B. Ozyilmaz, P. Kim, and K. L. Shepard, "Current saturation in zero-bandgap, top-gated graphene field-effect transistors," *Nat. Nanotechnol.* **3**, no. 11, 654, (2008).
- [12] R. Murali, Y. Yang, K. Brenner, T. Beck, and J. D. Meindl, "Breakdown current density of graphene nanoribbons," *Appl. Phys. Lett.*, **94**, no. 24, 243114, (2009).
- [13] C. Durkan & M. E. Welland, "Analysis of failure mechanisms in electrically-stressed gold nanowires", *Ultramicroscopy* **82**, 125 (2000).

- [14] J. Martin et al., "Observation of electron-hole puddles in graphene using a scanning single-electron transistor," *Nat. Phys.* **4**, no. 2, 144, (2008).
- [15] Z. Chen and J. Appenzeller, "Mobility extraction and quantum capacitance impact in high performance graphene field-effect transistor devices," *IEEE Int. Electron Dev. Meet.* **21**(1) 509 (2008).
- [16] H. E. Romero et al., "n-type behavior of graphene supported on Si/SiO₂ substrates," *ACS Nano*, **2**, no. 10, 2037, (2008).
- [17] H. Raza, "Edge and passivation effects in armchair graphene nanoribbons", *Phys Rev. B*. **84**, 165425 (2011).
- [18] "Introduction to COMSOL multiphysics®," *COMSOL Multiphysics, Burlington, MA*, vol. 9, p. 2018, 1998.
- [19] M. G. Ancona, "Electron transport in graphene from a diffusion-drift perspective," *IEEE Transactions on Electron Devices*, vol. 57, no. 3, pp. 681–689, 2010.
- [20] R. Jalilian, L. A. Jauregui, G. Lopez, J. Tian, C. Roecker, M. M. Yazdanpanah, R. W. Cohn, I. Jovanovic, and Y. P. Chen, "Scanning gate microscopy on graphene: charge inhomogeneity and extrinsic doping," *Nanotechnology*, **22**, 295705, (2011).
- [21] Md Ashiqur Rahman Lasker et al, "The enduring legacy of scanning spreading resistance microscopy: overview, advancements and future directions ", *Appl. Phys. Rev.* **12**, 041305 (2025)
- [22] A. Dey, A. Chroneos, N. St. J. Braithwaite, Ram P. Gandhiraman and S. Krishnamurthy, "Plasma engineering of graphene", *Appl. Phys. Rev.* **3**, 021301 (2016)
- [23] C. N. Bondja, Z. Geng, R. Granzner, J. Pezoldt, and F. Schwierz, "Simulation of 50-nm gate graphene nanoribbon transistors," *Electronics* **5**, 3 (2016).
- [24] J. Fang, W. G. Vandenberghe, and M. V Fischetti, "Microscopic dielectric permittivities of graphene nanoribbons and graphene," *Phys. Rev. B*, **94**, 45318, (2016).